Optimization of Synthetic Jet Position for Heat Transfer Enhancement and Temperature Uniformity of a Heated Wall in Micro-Channels

J. Khaleghinia[1], F. Kowsary[2†] and C. Aghanajafi[3]

[1]*Department of Mechanical and Aerospace Engineering, Science and Research Branch, Islamic Azad University, Tehran, Iran*
[2] *School of Mechanical Engineering, College of Engineering, University of Tehran, Tehran, Iran*
[3] *Department of Mechanical Engineering, K.N. Toosi University of Technology, Tehran, Iran*

†*Corresponding Author Email: fkowsari@ut.ac.ir*

ABSTRACT

In this study, the synthetic jet position was optimized to obtain the maximum rate of heat transfer and the best state of temperature uniformity on a heated surface in micro-channels. Based on micro-channel length, several cases were simulated to investigate the effects of synthetic jet position on the heat transfer rate and temperature uniformity. After that, the synthetic jet position was optimized using the CFD results and the GMDH-MOGA optimization code. The obtained results show that the synthetic jet placement in all longitudinal positions of micro-channel increases the heat transfer rate, although the improvement of temperature uniformity of heated surface decreases at some positions as compared to the micro-channel without synthetic jet. The optimization results show that for obtaining the maximum value of heat transfer and the best state of temperature uniformity on the heated surface, the dimensionless longitudinal position of synthetic should be between 0.45 and 0.65. The maximum rate of heat transfer and the best state of temperature uniformity have been observed in the vicinity of lower and upper bounds of this range, respectively.

Keywords: Micro-channel; Synthetic jet; Position; Optimization.

NOMENCLATURE

A	oscillation amplitude	T_P	period of oscillation
f	oscillation frequency		
L	microchannel length	T_s	wall temperature
L_C	cavity length	T_{s_ave}	average temperature of wall
P	pressure	X_{Jet}	synthetic jet position
q''	heat flux	X_R	improvement in temperature uniformity
t	time		
T	temperature	θ_R	improvement in temperature decrease
t^*	dimensionless time	σ	Standard deviation

1. INTRODUCTION

The quest for high performance microprocessors and consequently high power consumption and high heat generation have encountered the manufacturers with a significant challenge of heat dissipation. Moreover, the spatial and temporal power variations of the processors lead to non-uniformities in the temperature distribution as well. This causes high thermal stresses in the device which is detrimental to its performance and reliability (Liu *et al.*, 2005). Therefore, desired heat dissipation and obtaining temperature uniformity using modern cooling techniques can improve energy efficiency and performance coefficient.

Because of high heat generation in microelectronic equipment and low capacity of laminar airflow for heat transfer, it is necessary to use turbulent fluid

flow for cooling process (Qu *et al.*, 2000). Simultaneous use of water and synthetic jet for cooling is a new and interesting concept in which many researches are underway. This method increases the cooling capacity as compared to the air-cooling method. Synthetic jet consists of a cavity and a fluctuating membrane or reciprocating piston that is connected to the microchannel main flow using a slot, orifice or a small nozzle. The suction and blowing of the flow into and out of the cavity by membrane fluctuation or piston movement, increase the local momentum and cause turbulence in the microchannel flow.

Several studies have been carried out numerically as well as experimentally to investigate the effects of synthetic jets on the heat transfer process. Lee *et al.* (2005) investigated the thermal behavior of single-phase flow in a rectangular microchannel for several geometries and Reynolds numbers both experimentally and numerically. They reported a difference of 5% between the experimental and numerical results. Chaudhari *et al.* (2010) experimentally investigated the effect of the shape of the orifice of a synthetic jet on impingement cooling of a heated surface. They found that the heat transfer enhancement with a square orifice was larger than that with rectangular and circular shape at a large axial distance.

Lee *et al.* (2012) developed a three-dimensional computational model to investigate the interaction of two synthetic jets with cross flow in micro-channel. They found that the addition of one synthetic jet provides greater mixing of flow in the micro-channel than those with single synthetic jet. They also reported that the structure of the flow in micro-channel is strongly dependent on the period of the oscillation of the membrane of the synthetic jet actuator. Rylatt and O'Donovan (2013) experimentally investigated heat transfer to confined, un-ducted and ducted impinging synthetic air jets. They have shown that increasing the length of the confining plate reduces the cooling performance by up to 14% in the stagnation region and 8% on an area averaged basis.

Xia and Zhong (2014) enhanced the laminar flow mixing between two parallel water streams, which were injected into a rectangular channel using a pair of staggered lateral synthetic jets located on the opposite walls of the mixing channel. Their results have shown that an excellent mixing is obtained when a relatively high value of frequency or stroke length is used. Yu *et al.* (2014) experimentally and computationally investigated the integration of agitators and synthetic jet within air-cooled heat sink to significantly augment heat transfer performance. Their results have shown that the combination of the agitators and synthetic jets raises the heat transfer coefficient of channel by 82.4%, compared with the same channel having channel flow only. Yuan-Wei *et al.* (2014) investigated the effects of geometric parameters and excitation frequency of the actuator on the synthetic jet fluidic characteristics by utilizing a two-dimensional unsteady Reynolds-Averaged Navier-Stokes (URANS) model. They have shown that the geometric parameters of the actuator, such as the cavity depth and diameter, as well as orifice thickness and diameter, have important influences on the synthetic jet fluidic characteristics.

Lehnen *et al.* (2016) investigated the cooling effect of a single synthetic jet impinging directly on a heated surface in a 2-D numerical simulation. They examined several test cases involving changes in the distance between the heated surface and the jet source, jet Reynolds number, pulsing frequency and Prandtl number. They reported that the synthetic jet forms a circulation cell similar to a steady jet but with more fragmented vorticity. Jeng and Hsu (2016) experimentally examined the mixed convection heat transfer characteristics of a horizontal heated plate with the impinging cooling of down-blowing or up-blowing synthetic jet. Their experimental results showed that at a specified Reynods number, the Nusselt number of various models basically increased with relative impingement distance. They established an empirical Nusselt correlation of mixed convection in terms of Reynolds number and Grashof number at various relative impingement distances applicable to heat transfer analysis and optimal design of synthetic jet device.

The fundamental behavior of synthetic jet flow and its role in heat transfer enhancement have been investigated by Silva-Llanca *et al.* (2017). They proposed a new definition of the Reynolds number that represents the strength of the jet. They also reported that the jet-to-surface distance should be optimized based on vortex intensity. Effects of arrangement and phase difference of diaphragm oscillation of three synthetic jets on thermal behavior of flow in a microchannel have been studied numerically by Khaleghinia *et al.* (2017). They reported that the position of synthetic jets and their phase difference of oscillation are effective on heat transfer enhancement.

The position of the synthetic jet in a micro-channel is one of the important parameters that no consideration has been given to its optimal value yet. In the present study, the position of synthetic jet whose outflow interacts with the water cross-flow of micro-channel was optimized for the heat transfer enhancement and uniformity of temperature distribution on a heated surface based on micro-channel length variations.

2. NUMERICAL SIMULATION AND VALIDATION

In order to obtain the effects of synthetic jet position on heat transfer enhancement and temperature uniformity, four lengths of micro-channel in the range of 4 to 10mm, in which synthetic jet had operated at different longitudinal position, were simulated using two-dimensional numerical method. Numerical investigation has been performed using finite volume method in both laminar and turbulent flow regimes. Figure1 shows
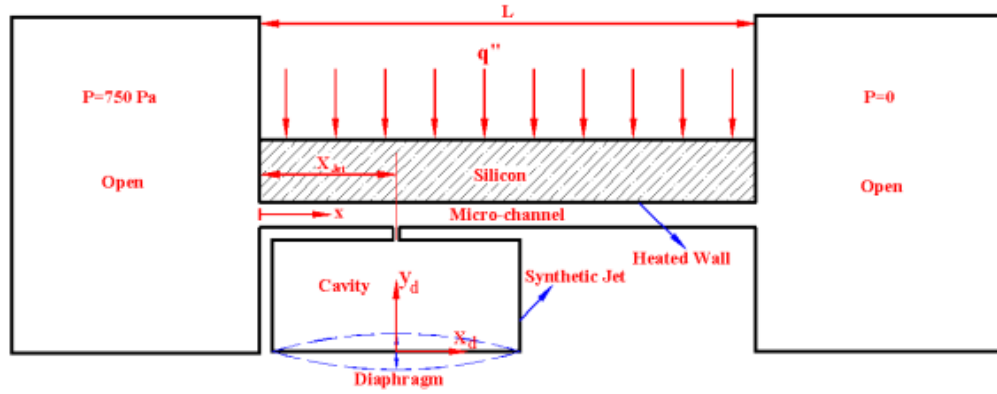
Fig. 1. Geometry of micro-channel and synthetic jet.

the parametric geometry of micro-channel and synthetic jet. All of the cases that were investigated numerically were listed in Table 1.

Table 1 Simulated cases based on micro-channel length and synthetic jet position

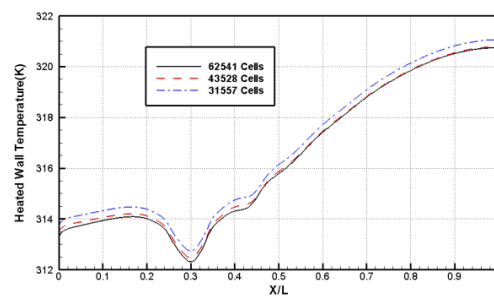| L(mm)	$\dfrac{X_{Jet}}{L}$
4	0.275, 0.350, 0.425, 0.500, 0.575, 0.650, 0.725
6	0.183, 0.289, 0.394, 0.500, 0.606, 0.711, 0.817
7	0.157, 0.271, 0.386, 0.500, 0.614, 0.729, 0.843
10	0.110, 0.240, 0.370, 0.500, 0.630, 0.760, 0.890

Governing equations including continuity equation, momentum equation and energy equation were solved using finite volume method. The SIMPLE algorithm was employed for the velocity-pressure coupling. The second order Upwind scheme was applied for the discretization of the convection term in the momentum equation. The four-equation SST turbulence model has been used to capture the turbulences in the flow field. Since the range of fluid temperature was not big, and its small effect on the fluid properties had no significant effect on the comparison results, the variation of fluid properties with temperature was ignored in this study. The converged solution of the steady state stage (micro-channel without synthetic jet) was used as the initial solution of the transient stage. The transient calculations started from the diaphragm stationary condition at $t^* = 0$, and diaphragm would reach to its highest and lowest point at $t^* = 0.25$ and $t^* = 0.75$, respectively. A dynamic mesh has been employed for the diaphragm oscillation according to:

$$y_d = A \left[1 - \left(\frac{x_d}{\frac{L_C}{2}} \right)^2 \right] \sin(2\pi f t) \qquad (1)$$

where x_d and y_d have been shown in Fig. 1 and L_C, A and f are the diaphragm length, oscillation amplitude and frequency, respectively. Dimensionless time variable is defined as:

$$t^* = \frac{t}{T_P}, \qquad (2)$$

where t indicates time and T_P represents the oscillation period of membrane. The grid size as well as time step size independency was investigated by comparing the temperature distribution over the heated wall for different mesh setups and several time step sizes (Figs. 2 and 3). The optimal mesh (43528 cells for $L=4mm$) and time step size ($T_p / 36$ for the all lengths) were chosen for the final analysis of flow field. This process has been repeated for all lengths of microchannel.

Fig. 2. Temperature distribution over the heated wall for several meshes ($L=4mm$, $X_{Jet}/L=0.275$).

The CFD results were compared to those of Sinclair *et al.* (2008) and Lee *et al.* (2012) for validation. Comparison of the variations of the centerline velocity and the circumferential Nusselt number over solid-fluid interface wall indicates a very good agreement between results (Figs. 4 and 5).

Figure 6 shows the vortices formation, their movement in the microchannel and their effects on the solid temperature. In the blowing stage, when the diaphragm moves toward the orifice, a pair of vortex rings are formed in the microchannel near the synthetic jet orifice (Fig. 6(a)). At the end of blowing stage, the diaphragm reaches to its maximum amplitude. The vortices collide with the heated wall with their maximum strength. The continuity of hydraulic and thermal boundary layers is interrupted by the vortices, and the temperature of heated wall decreases rapidly close to the collision region (Fig. 6(b)). The vortices should be away from the synthetic jet orifice before the starting of suction stage, otherwise, they can be ingested back into the cavity and the cooling performance of synthetic jet will be seriously decreased. With the starting of suction stage, the vortices will be weaker and gradually dissipate along the microchannel (Figs. 6(c) and (d)). These processes are repeated during the each cycle of oscillation of synthetic jet diaphragm.
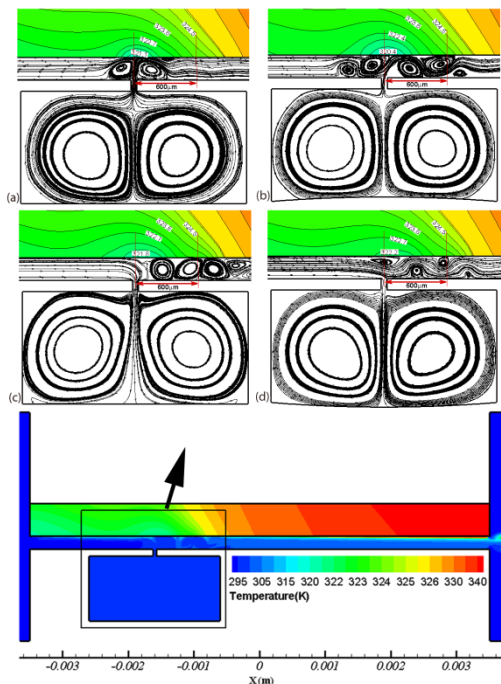

Fig. 6. Vortices formation and contour of temperature in Silicon during one period of diaphragm oscillation; (a): $t^* = 0$; (b): $t^* = 0.25$; (c): $t^* = 0.5$; (d): $t^* = 0.75$.

The CFD results show that the amount of heat transfer due to the synthetic jet performance is highly dependent on its location and the vortices strength. Figures 7 and 8 show the temperature distribution over the heated surface for two lengths of microchannel (*L=4mm* and *L=10mm*). In short microchannels, there is no sufficient length for the growth of interrupted boundary layer in the up- and downstream of synthetic jet location. The turbulence in the microchannel flow and the boundary layer interruption caused by the synthetic jet performance can lead to a decrease and uniformity in the

temperature of the heated surface at the both sides of synthetic jet location (Fig. 7). In almost all of these cases, the placement of synthetic jet in each longitudinal position of microchannel causes more decrease and better uniformity in the heated wall temperature as compared to the microchannel without synthetic jet.

If a synthetic jet is placed close to the inlet of a long microchannel, the interrupted boundary layer can redevelop in the downstream of synthetic jet location, and consequently, the surface temperature increases along the microchannel like as a microchannel without synthetic jet (Fig. 8). In a long microchannel where the synthetic jet has been located near its outlet, the boundary layer develops near the heated wall over a large length of microchannel in the upstream of synthetic jet. In addition, the vortices formed by the synthetic jet, leave microchannel rapidly. Thereby, the synthetic jet performance has no significant effect on the heat transfer enhancement. In these cases, the placement of synthetic jet in the middle region of the microchannel can somewhat prevent the boundary layer development and improve the heat transfer rate as compared to the microchannel without synthetic jet. Local cooling caused by the synthetic jet can lead to a decrease in the temperature uniformity of heated wall in long microchannels. To achieve a suitable temperature over a long heated surface, the use of two or more synthetic jet has been recommended.
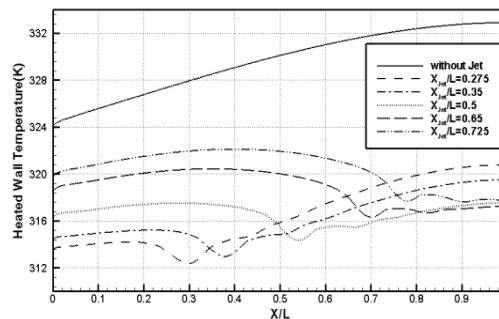
Fig. 7. Temperature distribution on the heated wall for length of L=4mm.
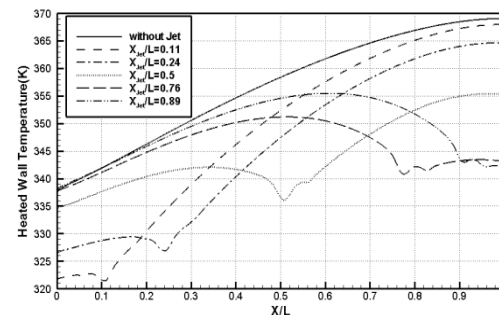
Fig. 8. Temperature distribution on the heated wall for length of L=10mm.

The average temperature and the difference between the local and average temperature of heated surface in each cycle of oscillation, have been considered to

compare the effects of synthetic jet location on heat transfer process. By comparison of average temperature of heated wall between two states in which synthetic jet is active or inactive, the relative decrease in average temperature is calculated as:

$$\theta_R = \left| \frac{T_{s\_ave\_unsteady} - T_{s\_ave\_steady}}{T_{s\_ave\_steady}} \right| \times 100 \ . \quad (3)$$

T_{s_ave} indicates the average temperature of the heated surface where is calculated as:

$$T_{s\_ave} = \frac{1}{L} \int_0^L T \, dx \ , \quad (4)$$

and unsteady and steady states refer to the states when the synthetic jet is active and inactive, respectively. In order to obtain the relative improvement in temperature uniformity, the standard deviation, which indicates the temperature deviation of different points of heated wall from its average temperature, is defined as:

$$\sigma = \sqrt{\frac{1}{L} \int_0^L \left(T_s(x) - T_{s\_ave} \right)^2 dx} \ . \quad (5)$$

The percentage of temperature uniformity, X , is calculated as:

$$X = \left| \frac{T_{s\_ave} - \sigma}{T_{s\_ave}} \right| \times 100 \ . \quad (6)$$

The relative improvement in temperature uniformity on the silicon-water interface wall, X_R , is calculated as:

$$X_R = \frac{X_{unstedy \ state} - X_{steady \ state}}{X_{steady \ state}} \ . \quad (7)$$

Table 2 shows the CFD results of θ_R and X_R for four lengths of micro-channel and seven different longitudinal positions of synthetic jet. For some positions of synthetic jet, especially in long microchannels, the value of X_R is negative. The negative sign of X_R indicates that the synthetic jet activity decreases the temperature uniformity of heated wall as compared to the microchannel without synthetic jet because of aforementioned reasons.

3. GROUP METHOD OF DATA HANDLING (GMDH) NEURAL NETWORK

The GMDH algorithm is the heuristic self-organization method which can be applied for forecasting and optimization of complex systems. This algorithm consists of several layers. In each layer different pairs of neurons are connected through a quadratic polynomial, and generate new neurons in the next layer. Each model can be presented by means of the generated neurons.

Table 2 CFD results of θ_R and X_R

L(mm)	$\frac{X_{Jet}}{L}$	θ_R	X_R
4	0.275	23.23	-1.78
4	0.350	23.76	0.20
4	0.425	23.72	2.04
4	0.500	22.89	2.85
4	0.575	21.35	2.31
4	0.650	19.12	1.62
4	0.725	16.25	1.33
6	0.183	18.17	-7.10
6	0.288	20.09	-4.18
6	0.393	20.92	-0.31
6	0.500	20.29	3.37
6	0.605	18.97	4.17
6	0.710	16.52	3.40
6	0.817	12.67	2.76
7	0.157	15.76	-8.76
7	0.271	18.28	-5.69
7	0.386	19.37	-1.01
7	0.500	19.06	3.93
7	0.614	17.96	5.56
7	0.729	15.59	4.51
7	0.843	11.54	3.86
10	0.110	9.58	-10.67
10	0.240	12.81	-8.62
10	0.370	14.40	-3.42
10	0.500	14.88	2.91
10	0.630	14.96	8.08
10	0.760	13.00	7.04
10	0.890	9.05	5.30

The GMDH method is a multi-layer algorithm in which a set of input-output data are connected to each other by Volterra function series. Unlike pairs in each layer are connected by a quadratic polynomial to generate new neurons in the next layer. The significant purpose of GMDH algorithm is to find a function f that can predict output y for a given input vector $X = (x_1, x_2, ..., x_n)$. The output is defined as:

$$y_i = f(x_{i1}, x_{i2}, ..., x_{in}); \ (i = 1, 2, ..., M) \quad (8)$$

where M is the number of calculated multi-input, single-output data pairs(Shirmohammadi *et al.*, 2015; Nariman-Zadeh *et al.*, 2005). GMDH-type neural network is then trained to predict the output values y_i for each given input vector $X = (x_{i1}, x_{i2}, ..., x_{in})$ as:

$$y_i = f(x_{i1}, x_{i2}, ..., x_{in}); \ (i = 1, 2, ..., M) \quad (9)$$

In order to obtain the acceptable predictions, the squared difference between the actual (CFD results) and predicted output must be minimized as:

$$\sum_{i=1}^{M} \left(y_i - y_i \right)^2 \rightarrow \min \ . \quad (10)$$

A complicated discrete form of Volterra series is utilized to obtain a general relation between input and output variables as:

$$y = a_0 + \sum_{i=1}^{n} a_i x_i + \sum_{i=1}^{n} \sum_{j=1}^{n} a_{ij} x_i x_j + \sum_{i=1}^{n} \sum_{j=1}^{n} \sum_{k=1}^{n} a_{ijk} x_i x_j x_k + ... , \tag{11}$$

which is known as the Kolmogorov-Gabor polynomial. For two variables, the above full form of mathematical description can be represented by a partial quadratic polynomial as follows:

$$y = G(x_i, x_j) = a_0 + a_1 x_i + a_2 x_j + a_3 x_i^2 + a_4 x_j^2 + a_5 x_i x_j \tag{12}$$

The above-mentioned partial quadratic description is used recursively to obtain the general mathematical relation between input and output variables. Regression techniques are utilized to calculate a_i values in Eq. (12). The difference between actual output and calculated one is minimized for each pair of input variables. For each row of M data triples, the following procedure is utilized to calculate.

$$Aa = Y ;$$
$$a = (a_0, a_1, ..., a_5); \; Y = (y_1, y_2, ..., y_M)^T \tag{13}$$

where a is the unknown vector and Y is the vector of output values. In order to calculate the vector of the best coefficients of the quadratic Eq. (12) for the all set of M data triples, the normal equations in the following form are used.

$$a = (A^T A)^{-1} A^T Y \tag{14}$$

This procedure is repeated in the next hidden layer for each neuron in accordance with the connectivity topology of the network. Singular Value Decomposition (SVD) is utilized to solve such linear least squares problems that some singularities might occur in the normal equations. This technique has been completely explained by Shirmohammadi *et al.* (2015).

Two types of the GMDH neural network are defined as CS-GMDH and GS-GMDH. In the CS-GMDH neural networks, the neurons only between adjacent layers are connected to each other (Fig. 9(a)). Whereas, In the GS-GMDH, each neuron in different layers can connect to the other neurons, which are not necessarily in the same layer (Fig. 9(b)). CS-GMDH and GS-GMDH neural networks can be transformed to each other using crossover and mutation processes (Nariman-Zadeh *et al.*, 2003; Shirmohammadi *et al.*, 2015).

4. GMDH-TYPE NEURAL NETWORK MODELLING OF HEAT TRANSFER IN MICRO-CHANNEL

The multiple input-single output data pairs used in the present work were obtained from CFD simulation. The inputs consist of three variables, namely the length of micro-channel (L), the dimensionless distant of the jet outlet from the micro-channel inlet (X_{Jet}/L) and the dimensionless distant of the jet outlet from the micro-channel outlet ($1 - X_{Jet}/L$), which the two recent variables are dependent on each other. The outputs consist of two variables, namely the relative decrease in average temperature (θ_R) and the relative improvement in temperature uniformity of heated wall (X_R).
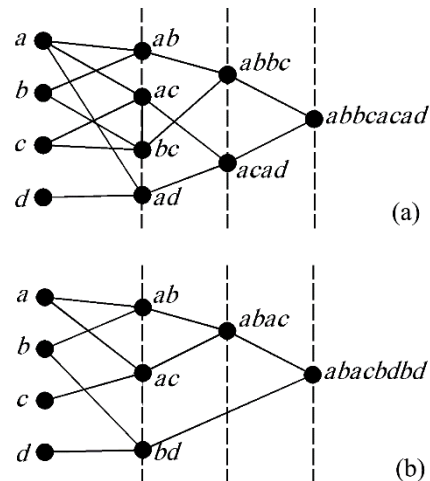

Fig. 9. Network structure of chromosome. (a)CS-GMDH type, (b)GS-GMDH type.

Table 2 includes of a total 28 data series, which have been calculated using numerical simulations to train and test such GMDH type neural networks. These data series have been employed for training and testing stages. In the training stage, the 21 of 28 data series which calculated for micro-channel lengths of *4mm*, *7mm* and *10 mm*, have been applied to derive a GS-GMDH algorithm. In the testing stage, the seven input-output data pairs in length of *6mm* that have not been used throughout the training process, were utilized for validating correlation obtained from the training process.

The structure of two hidden layer GS-GMDH-type neural network for θ_R and X_R are shown in Figs. 10 and 11, respectively.
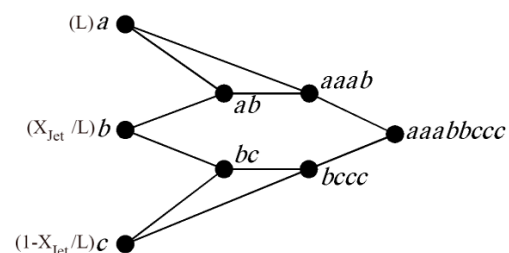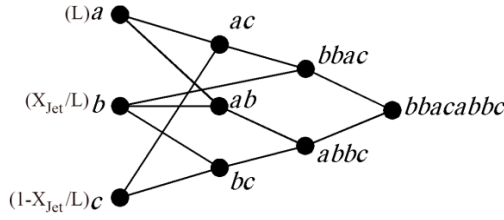

Fig. 10. Structure of GMDH-type neural network for relative decrease in average temperature.

Fig. 11. Structure of GMDH-type neural network for relative improvement in temperature uniformity.

The corresponding polynomial representation of θ_R is as:

$$y_1 = a_1 + a_2 x_1 + a_3 x_2 + a_4 x_1^2 + a_5 x_2^2 + a_6 x_1 x_2$$

$$y_2 = a_7 + a_8 x_2 + a_9 x_3 + a_{10} x_2^2 + a_{11} x_3^2 + a_{12} x_2 x_3$$

$$y_3 = a_{13} + a_{14} x_1 + a_{15} y_1 + a_{16} x_1^2 + a_{17} y_1^2 + a_{18} x_1 y_1 \qquad (15)$$

$$y_4 = a_{19} + a_{20} y_2 + a_{21} x_3 + a_{22} y_2^2 + a_{23} x_3^2 + a_{24} y_2 x_3$$

$$\theta_R = a_{25} + a_{26} y_3 + a_{27} y_4 + a_{28} y_3^2 + a_{29} y_4^2 + a_{30} y_3 y_4$$

where x_1, x_2 and x_3 stand for L, X_{Jet}/L and $1 - X_{Jet}/L$, respectively, and the constants are as:

a_1 =28.171	a_{11} =-18.053	a_{21} =-7.684
a_2 =-2.310	a_{12} =26.903	a_{22} =-0.030
a_3 =18.910	a_{13} =-18.766	a_{23} =-8.260
a_4 =-0.004	a_{14} =2.701	a_{24} =1.140
a_5 =-42.984	a_{15} =2.148	a_{25} =-0.604
a_6 =2.429	a_{16} =-0.091	a_{26} =0.237
a_7 =15.319	a_{17} =-0.017	a_{27} =0.825
a_8 =6.468	a_{18} =-0.086	a_{28} =-0.013
a_9 =8.851	a_{19} =0.186	a_{29} =-0.053
a_{10} =-20.435	a_{20} =1.309	a_{30} =0.064

Similarly, the corresponding polynomial representation of X_R is as:

$$y_1 = a_1 + a_2 x_1 + a_3 x_3 + a_4 x_1^2 + a_5 x_3^2 + a_6 x_1 x_3$$

$$y_2 = a_7 + a_8 x_1 + a_9 x_2 + a_{10} x_1^2 + a_{11} x_2^2 + a_{12} x_1 x_2$$

$$y_3 = a_{13} + a_{14} x_2 + a_{15} x_3 + a_{16} x_2^2 + a_{17} x_3^2 + a_{18} x_2 x_3$$

$$y_4 = a_{19} + a_{20} y_1 + a_{21} x_2 + a_{22} y_1^2 + a_{23} x_2^2 + a_{24} y_1 x_2$$

$$y_5 = a_{25} + a_{26} y_2 + a_{27} y_3 + a_{28} y_2^2 + a_{29} y_3^2 + a_{30} y_2 y_3$$

$$X_R = a_{31} + a_{32} y_4 + a_{33} y_5 + a_{34} y_4^2 + a_{35} y_5^2 + a_{36} y_4 y_5 \qquad (16)$$

where

a_1 =-10.414	a_{13} =3.509	a_{25} =-0.667
a_2 =1.646	a_{14} =6.822	a_{26} =1.162
a_3 =44.998	a_{15} =-3.313	a_{27} =0.006
a_4 =-0.008	a_{16} =-7.786	a_{28} =-0.156
a_5 =42.983	a_{17} =-17.920	a_{29} =-0.148
a_6 =-2.803	a_{18} =14.607	a_{30} =0.340
a_7 =-8.399	a_{19} =11.189	a_{31} =-0.227
a_8 =-1.157	a_{20} =-46.195	a_{32} =1.0310
a_9 =40.967	a_{21} =3.843	a_{33} =-0.001
a_{10} =-0.008	a_{22} =43.334	a_{34} =0.342
a_{11}	a_{23} =0.149	a_{35} =0.336
a_{12} =2.803	a_{24} =-5.124	a_{36} =-0.681

A very good agreement between such GMDH-type neural network model and CFD results for the training and testing data was shown in Figs. 12 and 13. These figures also show that the obtained correlations successfully predict the outputs of testing data that have not been applied during the training process.

The correlations obtained in this section can now be used for Pareto multi-objective optimization of θ_R and X_R in a micro-channel with different lengths in which a synthetic jet operates at different longitudinal positions.
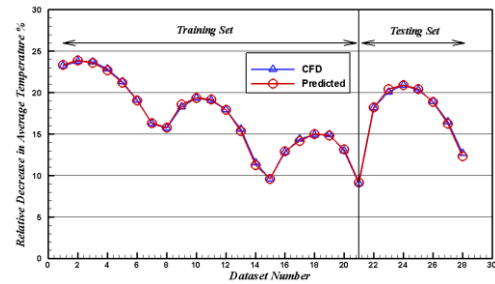
Fig. 12. Variations of relative decrease in average temperature of heated wall.
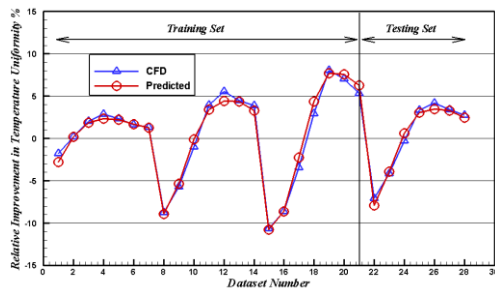
Fig. 13. Variations of relative improvement in temperature uniformity of heated wall.
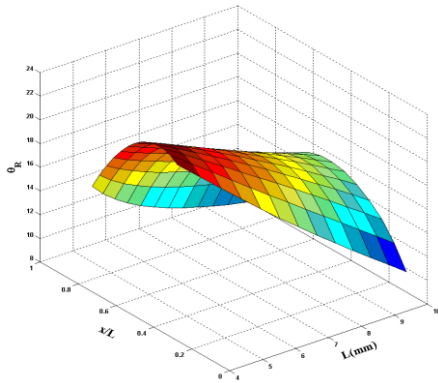
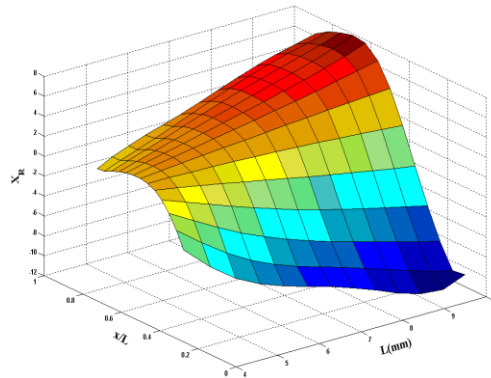**Fig. 14. Variations of relative decrease in average temperature of heated wall.**

Fig. 15. Variations of relative improvement in the temperature uniformity of heated wall.
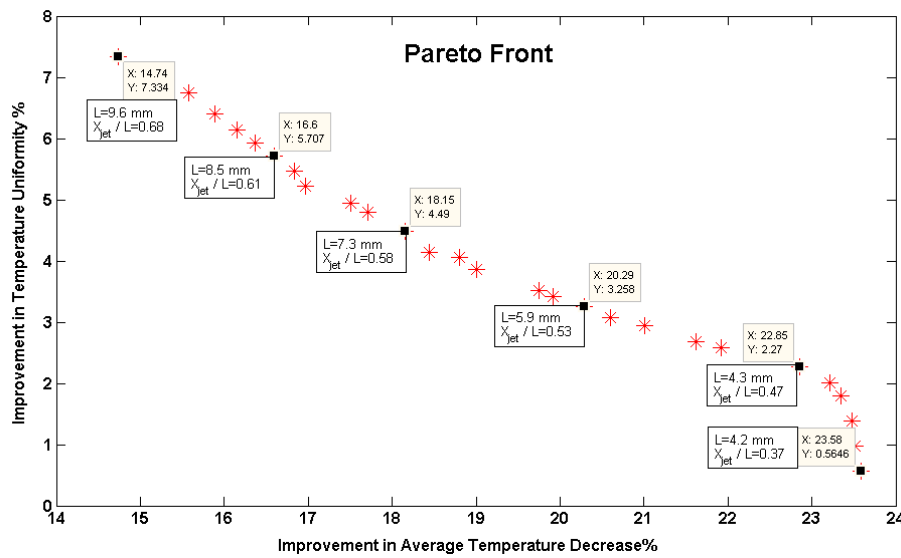

Fig. 16. Pareto front of improvement of temperature decrease and temperature uniformity of heated wall.

5. MULTI-OBJECTIVE OPTIMIZATION

Multi-objective optimization has been defined as finding a vector of decision variables satisfying constraints to give acceptable values to all objective functions (Deb *et al.*, 2002). In this paper, two such objectives, namely θ_R and X_R are considered simultaneously for multi-objective optimization. Both the two objective functions should be maximized in a certain range of micro-channel length and dimensionless longitudinal positions of synthetic jet as:

$$Objective\ functions \begin{cases} Z_1 = Maximize\ \theta_R(Y) \\ Z_2 = Maximize\ X_R(Y) \\ Y = \left(L, \dfrac{X_{Jet}}{L}, 1 - \dfrac{X_{Jet}}{L}\right) \end{cases}$$

$$Constraints: \begin{cases} 4(mm) \leq L \leq 10(mm) \\ 0.11 \leq \dfrac{X_{Jet}}{L} \leq 0.89 \end{cases} \tag{17}$$

Figures 14 and 15 show that the heat transfer rate due to synthetic jet has decreased with increase of micro-channel length in the range of *4 to 10 mm*, but the temperature uniformity has increased in the same range, instead. These figures also show that the best dimensionless position of synthetic jet is about 0.4 to 0.7. This was confirmed by Pareto front obtained from the multi-objective optimization model (Fig. 16). Moreover, the maximum value of heat transfer rate has been observed in the vicinity of X_{Jet}/L equal to 0.4, and its value has decreased with increase of X_{Jet}/L as has been illustrated in Fig. 16. In the vicinity of X_{Jet}/L equal to 0.7, the heat transfer rate and the temperature uniformity reached to their minimum and maximum values, respectively. Therefore, the Pareto front can be used to obtain the optimum position of synthetic jet in the micro-channel.

6. CONCLUSION

The position of a synthetic jet has been optimized using numerical results in micro-channels. At first, the flow field and heat transfer of four micro-channels with different lengths equipped with a synthetic jet have been investigated numerically. Then, the position of synthetic jet has been optimized using CFD results, GMDH method and GA algorithm to obtain the maximum heat transfer rate and best state of temperature uniformity of a heated wall. The heat transfer rate and the temperature uniformity of heated wall have been changed by the changes of synthetic jet position from micro-channel inlet to its outlet. Placement of synthetic jet in the vicinity of the micro-channel inlet and outlet, had no much effect on the heat transfer process as compared to micro-channel without synthetic jet. The effects of synthetic jet were noticeable in a certain range of micro-channel length. This range for the dimensionless ratio of X_{Jet}/L was between 0.4 and 0.7 in the microchannels with a length of 4 to 10mm.

REFERENCES

Chaudhari, M., B. Puranik and A. Agrawal (2010). Effect of orifice shape in synthetic jet based impingement cooling. *Experimental Thermal and Fluid Science* 34(2), 246–256.

Deb, K., A. Pratap, S. Agarwal and T. Meyarivan (2002). A fast and elitist multiobjective genetic algorithm: NSGA-II. *IEEE Transactions on Evolutionary Computation* 6(2), 182–197.

Jeng, T. M. and W. T. Hsu (2016). Experimental study of mixed convection heat transfer on the heated plate with the circular-nozzle synthetic jet. *International Journal of Heat and Mass Transfer* 97, 559–568.

Khaleghinia, J., F. Kowsary and C. Aghanajafi (2017). Effects of arrangement and phase difference of oscillation of synthetic jets on heat transfer in micro-channels. *Mechanika* 23(1), 78–83.

Lee, A., V. Timchenko, G. H. Yeoh and J. A. Reizes (2012). Three-dimensional modelling of fluid flow and heat transfer in micro-channels with synthetic jet. *International Journal of Heat and Mass Transfer* 55(1–3), 198–213.

Lee, P.-S., S. V. Garimella and D. Liu (2005). Investigation of heat transfer in rectangular microchannels. *International Journal of Heat and Mass Transfer* 48(9), 1688–1704.

Lehnen, M. V., C. Y. Y. Lee and F. L. D. Alves (2016). Nusselt number correlation for synthetic jets. *Journal of the Brazilian Society of Mechanical Sciences and Engineering* 38(7), 2161–2171.

Liu, P., Z. Qi, H. Li, L. Jin, W. Wu, S. X. D. Tan and J. Yang (2005). Fast thermal simulation for architecture level dynamic thermal management. IEEE/ACM International Conference on Computer-Aided Design, 2005, 638-643.

Nariman-Zadeh, N., A. Darvizeh and G. R. Ahmad-Zadeh (2003). Hybrid genetic design of GMDH-type neural networks using singular value decomposition for modelling and prediction of the explosive cutting process. *Proceedings of the Institution of Mechanical Engineers, Part B: Journal of Engineering Manufacture* 217(6), 779–790.

Nariman-Zadeh, N., A. Darvizeh, A. Jamali and A. Moeini (2005). Evolutionary design of generalized polynomial neural networks for modelling and prediction of explosive forming process. *Journal of Materials Processing Technology* 165, 1561–1571.

Qu, W., G. M. Mala and D. Li (2000). Heat transfer for water flow in trapezoidal silicon microchannels. *International Journal of Heat and Mass Transfer* 43(21), 3925–3936.

Rylatt, D. I. and T. S. O. Donovan (2013). Heat transfer enhancement to a con fi ned impinging synthetic air jet. *Applied Thermal Engineering* 51(1–2), 468–475.

Shirmohammadi, R., B. Ghorbani, M. Hamedi, M. H. Hamedi and L. M. Romeo (2015). Optimization of mixed refrigerant systems in low temperature applications by means of group method of data handling (GMDH). *Journal of Natural Gas Science and Engineering* 26, 303–312.

Silva-Llanca, L., J. Paul d'Alençon and A. Ortega (2017). Vortex dynamics-driven heat transfer and flow regime assessment in a turbulent impinging synthetic jet. *International Journal of Thermal Sciences* 121, 278–293.

Sinclair, A., V. Timchenko, J. Reizes, G. Rosengarten and E. Leonardi (2008). An Experimental and Numerical Study of a Micro-Synthetic Jet in a Shallow Cavity, in: *ASME 2008 6th International Conference on Nanochannels, Microchannels, and Minichannels*, ASME, 1195–1201.

Xia, Q. and S. Zhong (2014). Enhancement of laminar flow mixing using a pair of staggered lateral synthetic jets. *Sensors and Actuators, A: Physical* 207, 75–83.

Yu, Y., T.W. Simon, M. Zhang, T. Yeom, M. T. North and T. Cui (2014). Enhancing heat transfer in air-cooled heat sinks using piezoelectrically- driven agitators and synthetic jets. *International Journal of Heat and Mass Transfer* 68, 184–193.

Yuan Wei, L., Z. Jing Zhou, S. Yong and T. Xiao Ming (2014). Numerical investigation for effects of actuator parameters and excitation frequencies on synthetic jet fluidic characteristics. *Sensors and Actuators, A: Physical* 219, 100–111.